Results of Benchmark Problems for the Third Computational Aeroacoustics Workshop

Fang Q. Hu
Department of Mathematics and Statistics
Old Dominion University, Norfolk, VA 23529
E-mail: fang@math.odu.edu

Introduction

Numerical results for problems in Category 1, 2 and 5 are presented. Due to high resolution requirements of these problems, high-order finite difference schemes are used. Both the spatial and temporal discretizations have been optimized for obtaining low dissipation and low dispersion errors in computation. In addition, Perfectly Matched Layers (PML) are used at all non-reflecting boundaries encountered in Categories 2 and 3. The schemes used in the present work are modified from those for the benchmark problems in the previous two CAA workshops [1,2]. Further details of the algorithms are referred to [1] and [2].

Propagation of sound waves through transonic nozzle

In this problem, an acoustic wave is introduced at the nozzle exit region and the sound wave that travels upstream through the transonic nozzle is to be calculated. The amplitude of the incoming sound wave is 10^{-5} , which is very small compared to the mean values of the flow. The nozzle flow is modeled by the one-dimensional Euler equations with variable nozzle area. In the present work, the acoustic wave will be computed directly by solving the non-linear governing equations, rather than solving the linearized equations. This makes it harder to compute the acoustic waves. The challenge is whether the small amplitude wave can still be captured in the computation.

The governing equations are

$$\frac{\partial \rho}{\partial t} + u \frac{\partial \rho}{\partial x} + \rho \frac{\partial u}{\partial x} + \frac{\rho u}{A} \frac{\partial A}{\partial x} = 0 \tag{1}$$

$$\frac{\partial u}{\partial t} + u \frac{\partial u}{\partial x} + \frac{1}{\rho} \frac{\partial p}{\partial x} = 0 \tag{2}$$

$$\frac{\partial p}{\partial t} + u \frac{\partial p}{\partial x} + \gamma p \frac{\partial u}{\partial x} + \frac{\gamma p u}{A} \frac{\partial A}{\partial x} = 0$$
 (3)

where ρ is the density, u is the velocity and p is the pressure. A in (1)-(3) is the nozzle area and is a function of x given by

$$A(x) = \begin{cases} 0.536572 - 0.19808e^{-(\ln 2)\left(\frac{x}{0.6}\right)^2}, & x > 0\\ 1.0 - 0.661514e^{-(\ln 2)\left(\frac{x}{0.6}\right)^2}, & x < 0 \end{cases}$$

The computational domain is $-10 \le x \le 10$. An upstream propagating wave with very small amplitude is introduced at the nozzle exit region in the form of

$$\begin{bmatrix} \rho \\ u \\ p \end{bmatrix}_{\text{accoustic}} = 10^{-5} \begin{bmatrix} 1 \\ -1 \\ 1 \end{bmatrix} \cos \left[\omega \left(\frac{x}{1 - M} + t \right) \right] \tag{4}$$

When propagating upstream, part of the wave will be reflected at the nozzle throat and the other part is transmitted which travels to the left and leaves the inlet region of the nozzle. The mean values at the exit region are given,

$$\bar{\rho}_{exit} = 1.0, \ \bar{u}_{exit} = 0.4, \ \bar{p}_{exit} = 1/\gamma$$

To solve (1)-(3), boundary conditions are needed at the nozzle inlet and exit. At the inlet, there is a only left traveling wave and at the exit, there are left traveling incoming wave (given in (4)) and its reflection by the nozzle throat, a right traveling wave. The necessary numerical boundary conditions can be obtained in several ways. One approach is to rewrite the non-linear equations (1)-(3) in characteristics form and add the incoming wave as source terms [3, 4, 5]. In the present work, we derived the boundary equations based on the characteristics of the linearized equations of (1)-(3) since the wave amplitude is very small. We note that the linearization is only applied at the exit and inlet regions where the nozzle area is constant.

let

$$\rho = \bar{\rho} + \rho'$$

$$u = \bar{u} + u'$$

$$p = \bar{p} + p'$$

where an overbar indicates the time-independent mean value. Since now A = constant, we linearize equations (1)-(3) and write in the matrix form,

$$\frac{\partial}{\partial t} \begin{pmatrix} \rho' \\ u' \\ p' \end{pmatrix} + \begin{pmatrix} \bar{u} & \bar{\rho} & 0 \\ 0 & \bar{u} & \frac{1}{\bar{\rho}} \\ 0 & \gamma \bar{p} & \bar{u} \end{pmatrix} \frac{\partial}{\partial x} \begin{pmatrix} \rho' \\ u' \\ p' \end{pmatrix} = 0$$
 (5)

The coefficient matrix can be easily diagonalized,

$$\frac{\partial}{\partial t} \begin{pmatrix} \rho' \\ u' \\ p' \end{pmatrix} + \begin{pmatrix} 1 & \frac{\bar{\rho}}{\gamma \bar{\rho}} & \frac{\bar{\rho}}{\gamma \bar{\rho}} \\ 0 & \frac{1}{\bar{\rho} \bar{a}} & -\frac{1}{\bar{\rho} \bar{a}} \\ 0 & 1 & 1 \end{pmatrix} \begin{pmatrix} \bar{u} & 0 & 0 \\ 0 & \bar{u} + \bar{a} & 0 \\ 0 & 0 & \bar{u} - \bar{a} \end{pmatrix} \begin{pmatrix} 1 & 0 & -\frac{\bar{\rho}}{\gamma \bar{\rho}} \\ 0 & \frac{\bar{\rho} \bar{a}}{2} & \frac{1}{2} \\ 0 & -\frac{\bar{\rho} \bar{\rho}}{2} & \frac{1}{2} \end{pmatrix} \frac{\partial}{\partial x} \begin{pmatrix} \rho' \\ u' \\ p' \end{pmatrix} = 0$$
(6)

where $\bar{a} = \sqrt{\frac{\gamma \bar{p}}{\bar{\rho}}}$ is the speed of sound and \bar{u} , $\bar{u} + \bar{a}$, $\bar{u} - \bar{a}$ are the eigenvalues.

Boundary conditions can now be formulated using (6). At the inlet, let

$$\rho = \bar{\rho}_{inlet} + \rho'$$

$$u = \bar{u}_{inlet} + u'$$

$$p = \bar{p}_{inlet} + p'$$

where ρ' , u', p' are the out-going (traveling to the left) waves. The equations for ρ' , u', p' are found by keeping only the negative eigenvalue in the characteristics form (6), namely $\bar{u} - \bar{a}$. It follows that

$$\frac{\partial \rho'}{\partial t} - \frac{(\bar{u}_{inlet} - \bar{a}_{inlet})\bar{\rho}_{inlet}}{2\bar{a}_{inlet}} \frac{\partial u'}{\partial x} + \frac{\bar{u}_{inlet} - \bar{a}_{inlet}}{2\bar{a}_{inlet}^2} \frac{\partial p'}{\partial x} = 0 \tag{7}$$

$$\frac{\partial u'}{\partial t} + \frac{\bar{u}_{inlet} - \bar{a}_{inlet}}{2} \frac{\partial u'}{\partial x} - \frac{\bar{u}_{inlet} - \bar{a}_{inlet}}{2\bar{\rho}_{inlet}\bar{a}_{inlet}} \frac{\partial p'}{\partial x} = 0$$
 (8)

$$\frac{\partial \rho'}{\partial t} - \frac{(\bar{u}_{inlet} - \bar{a}_{inlet})\bar{\rho}_{inlet}\bar{a}_{inlet}}{2} \frac{\partial u'}{\partial x} + \frac{\bar{u}_{inlet} - \bar{a}_{inlet}}{2} \frac{\partial p'}{\partial x} = 0$$
 (9)

Similarly, at the outlet, we decompose the variables as

$$\rho = \bar{\rho}_{exit} + \rho_a + \rho'$$

$$u = \bar{u}_{exit} + u_a + u'$$

$$p = \bar{p}_{exit} + p_a + p'$$

where ρ_a , u_a and p_a are the incoming wave as specified in (4) and p', u' and p' represent the right traveling out-going wave (reflection by the nozzle throat). By only keeping positive eigenvalues in the characteristics equations (6), namely \bar{u} and $\bar{u} + \bar{a}$, we get following equations,

$$\frac{\partial \rho'}{\partial t} + \bar{u}_{exit} \frac{\partial \rho'}{\partial x} + \frac{(\bar{u}_{exit} + \bar{a}_{exit})\bar{\rho}_{exit}}{2\bar{a}_{exit}} \frac{\partial u}{\partial x} - \frac{\bar{u}_{exit} - \bar{a}_{exit}}{2\bar{a}_{exit}^2} \frac{\partial p'}{\partial x} = 0$$
 (10)

$$\frac{\partial u'}{\partial t} + \frac{\bar{u}_{exit} + \bar{a}_{exit}}{2} \frac{\partial u'}{\partial x} + \frac{\bar{u}_{exit} + \bar{a}_{exit}}{2\bar{\rho}_{exit}\bar{a}_{exit}} \frac{\partial p'}{\partial x} = 0$$
(11)

$$\frac{\partial p'}{\partial t} + \frac{(\bar{u}_{exit} + \bar{u}_{exit})\bar{\rho}_{exit}\bar{u}_{exit}}{2} \frac{\partial u'}{\partial x} + \frac{\bar{u}_{exit} + \bar{u}_{exit}}{2} \frac{\partial p'}{\partial x} = 0$$
 (12)

In the present calculation, Euler equations (1)-(3) are applied in -8 < x < 8. The inlet and exit boundary conditions, (7)-(9) and (10)-(12), are applied in $-10 \le x \le -8$ and $8 \le x \le 10$ respectively, as shown in Figure 1. The partitioning for these domains is somewhat arbitrary, so long as the nozzle areas are constant inside the boundary zones.

The spatial discretizations is carries out using a non-uniform grid with $\Delta x_{min} = 0.0125$ and $\Delta x_{max} = 0.1$ and a total of 381 grid points. The central differencing scheme used is the same as that of [6]. The time integration is carried out by the Low Dissipation and Low-Dispersion Runge-Kutta scheme (LDDRK56 [7]) with a time step $\Delta t = 0.0076$.

The initial values of the density, velocity and pressure are formed by a simple linear distribution, as shown in Figure 2 in dashed lines. As time increases, the solution adjusts itself for the given nozzle shape and mean values at the inlet and exit. The solid line in Figure 2 show the the density, velocity and pressure distribution at t = 200. Figure 3 shows a time sequence of the pressure distribution. This is to demonstrate that the transient responses propagate out of the computational domain very effectively. Figure 4 shows the pressure as a

function of time at x=-8, 0 and 8 respectively. Clearly, time periodic solution is reached after about t=100. In the present calculation, the acoustic wave is computed directly from the non-linear equations (1)-(3) and together with the mean flow. It shows that despite the small amplitude of the wave, the scheme can still capture the wave. After subtracting the mean value, the acoustic wave is found and the wave envelope is shown in Figure 5.

Shock-Sound Interaction

In this problem, the pressure at the exit is specified such that a shock is formed inside the nozzle. The mean velocity at the inlet is now given as $\bar{u}_{inlet} = 0.2006533$ and the pressure at the exit is,

$$\bar{p}_{exit} = 0.6071752$$

The governing equations are the same as that in the previous section, namely (1)-(3). An incoming wave is given in the inlet in the form of

$$\begin{bmatrix} \rho \\ u \\ p \end{bmatrix}_{accustic} = 10^{-5} \begin{bmatrix} 1 \\ 1 \\ 1 \end{bmatrix} \sin \left[\omega \left(\frac{x}{1+M} - t \right) \right]$$

Numerically, this problem is solved in a similar manner as in the previous one. At the inlet region, we let

$$\begin{bmatrix} \rho \\ u \\ p \end{bmatrix} = \begin{bmatrix} \bar{\rho}_{inlet} \\ \bar{u}_{inlet} \\ \bar{p}_{inlet} \end{bmatrix} + \begin{bmatrix} \rho_a \\ u_a \\ p_a \end{bmatrix} + \begin{bmatrix} \rho' \\ u' \\ p' \end{bmatrix}$$

and ρ' , u' and p' are solved using (7)-(9). At the exit region, we let

$$\begin{bmatrix} \rho \\ u \\ p \end{bmatrix} = \begin{bmatrix} \bar{\rho}_{exit} \\ \bar{u}_{exit} \\ \bar{p}_{exit} \end{bmatrix} + \begin{bmatrix} \rho' \\ u' \\ p' \end{bmatrix}$$

and ρ' , u' and p' are solved using (10)-(12).

Time history of pressure variation in x is shown in Figure 6 which exhibits in detail the formation of the shock. The final profiles of density, velocity and pressure are given Figure 7. Clearly, there are oscillations near the shock. Since a central difference scheme is used in the present calculation, the oscillations near the shock are not unexpected. Artificial dissipation terms have been introduced in the discretized equations. The magnitude of the artificial viscosity used at each grid point is set to be proportional to the maximum variation of the solution near the point. Again, non-uniform grids are used with $\Delta x_{min} = 0.003125$ and $\Delta x_{max} = 0.1$ with a total of 617 points. As a results, the oscillations near the shock are limited to a very narrow region as shown in Figure 7.

The emphasis of the current calculation is to see whether the small acoustic disturbance can still be accurately computed despite the inaccuracy near the shock. The results are satisfactory. Time periodic solutions are obtained after around t = 80 as shown in Figure 8 where pressure as a function of time at x = -8, 0

and 8 are given. The small acoustic wave is again captured directly from the non-linear equations (1)-(3). By subtracting the numerical solution by its mean value, wave envelop is found and shown in Figure 9. We see that despite the high spike of the wave near the shock, the transmitted and reflected sound waves are quite accurate.

Rotor Noise

In this problem, sound generated by an 8-blade rotor is simulated. Two cases are considered. The first is an open rotor and the second is a ducted rotor. The rotor is modeled by introducing forcing terms to the governing equations as specified in the problem,

$$\frac{\partial u}{\partial t} + \frac{\partial p}{\partial x} = F_x
\frac{\partial v}{\partial t} + \frac{\partial p}{\partial r} = F_r
\frac{\partial w}{\partial t} + \frac{1}{r} \frac{\partial p}{\partial \phi} = F_{\phi}
\frac{\partial p}{\partial t} + \frac{\partial u}{\partial x} + \frac{\partial v}{\partial r} + \frac{v}{r} + \frac{1}{r} \frac{\partial w}{\partial \phi} = 0$$
(13)

where the forcing terms are given as follows,

$$\begin{pmatrix} F_x \\ F_r \\ F_{\phi} \end{pmatrix} = \mathbf{Re} \left\{ \begin{pmatrix} \mathbf{J_m}(\lambda_{\mathbf{m}}\mathbf{r})e^{-(\ln 2)(10x)^2} \\ 0 \\ \mathbf{J_m}(\lambda_{\mathbf{m}}\mathbf{r})re^{-(\ln 2)(10x)^2} \end{pmatrix} e^{i\mathbf{m}(\phi - \Omega t)} \right\}$$

Here, **m** represents the number of blades. Equation (13) is further reduced to a 2-D problem by factoring out the ϕ dependency of the solution,

$$\begin{bmatrix} u \\ v \\ w \\ p \end{bmatrix} = Re \left\{ \begin{bmatrix} \tilde{u} \\ \tilde{v} \\ \tilde{w} \\ \tilde{p} \end{bmatrix} e^{im\phi} \right\}$$

and we get, in complex variables,

$$\frac{\partial \tilde{u}}{\partial t} + \frac{\partial \tilde{p}}{\partial x} = S(r)e^{-(\ln 2)(10x)^2}e^{-im\Omega t}$$

$$\frac{\partial \tilde{v}}{\partial t} + \frac{\partial \tilde{p}}{\partial r} = 0$$

$$\frac{\partial \tilde{w}}{\partial t} + \frac{im\tilde{p}}{r} = rS(r)e^{-(\ln 2)(10x)^2}e^{-im\Omega t}$$

$$\frac{\partial \tilde{p}}{\partial t} + \frac{\partial \tilde{u}}{\partial x} + \frac{\partial \tilde{v}}{\partial r} + \frac{\tilde{v}}{r} + \frac{im\tilde{w}}{r} = 0$$
(14)

where

$$S(r) = \begin{cases} \mathbf{J_m}(\lambda_{\mathbf{mN}}r), & r \le 1\\ 0, & r > 1 \end{cases}$$

in which $J_{\mathbf{m}}$ is the Bessel function of order \mathbf{m} and $\lambda_{\mathbf{mN}}$ is the \mathbf{N} th root of $J'_{\mathbf{m}}$. For the problem specified, $\mathbf{m}=8$ and $\mathbf{N}=1$ and $\lambda_{8,1}=9.64742$.

Open Rotor

For the open rotor case, the computational domain of $[-9, 9] \times [0, 9]$ is shown in Figure 10. Spatial derivatives in (14) are discretized by a 7-point optimized central difference scheme (as in the DRP scheme [5]) using a uniform grid of $\Delta x = \Delta y = 0.05$. The time integration is carried out by the Low-Dissipation and Low-Dispersion Runge-Kutta scheme (LDDRK56 [7]) with a time step $\Delta t = 0.025$. In addition, a tenth-order explicit filter is applied throughout the computational domain [2,9].

Perfectly Matched Layer (PML) equations are used at non-reflecting boundaries of the problem shown in Figure 10. The width of the PML domain is 1. Inside the PML domain, the pressure \tilde{p} is split into two parts and the following equations are solved:

$$\tilde{p} = \tilde{p}_1 + \tilde{p}_2$$

$$\frac{\partial \tilde{p}_1}{\partial t} + \sigma_x \tilde{p}_1 + \frac{\partial \tilde{u}}{\partial x} = 0$$

$$\frac{\partial \tilde{p}_2}{\partial t} + \sigma_r \tilde{p}_2 + \frac{\partial \tilde{v}}{\partial r} + \frac{\tilde{v}}{r} + \frac{i \mathbf{m} \tilde{w}}{r} = 0$$

in which σ_x and σ_r are the absorption coefficients introduced for absorbing the waves that enter the PML domain. The choice of the absorption coefficients follows a "matched" manner [8, 9]. At the right and the left PML domains in Figure 9, $\sigma_r = 0$ and at the top PML domain, $\sigma_x = 0$. At the corner regions, both coefficients are not zero. Specifically, the magnitudes of the absorption coefficients vary smoothly inside the PML domain as follows,

$$\sigma_x = \sigma_{max} \left(\frac{x - x_0}{D}\right)^2$$

$$\sigma_r = \sigma_{max} \left(\frac{r - r_0}{D}\right)^2$$

where x_0 and r_0 are the location of the initial positions of the PML domain and D is the width of the PML domain. In all calculations, $\sigma_{max}\Delta x = 2$.

At the centerline r = 0,

$$\tilde{v} = \tilde{w} = \tilde{p} = 0$$

and singular terms in equation (14) are replaced by partial derivative terms using L'Hospital's Rule, namely,

$$\frac{\tilde{v}}{r} = \frac{\partial \tilde{v}}{\partial r}, \ \frac{\tilde{w}}{r} = \frac{\partial \tilde{w}}{\partial r}, \ \frac{\tilde{p}}{r} = \frac{\partial \tilde{p}}{\partial r}$$

at r=0.

Pressure contours are shown in Figure 11 (a) and (b) for $\Omega = 0.85$ and 1.15 respectively. To show that a time periodic state has been reached, the pressure as function of time at point (0, 8.5) is shown in Figure 12. We note that although the pressure contours show similar patterns of sound radiation for both cases, the

intensities are quite different. The second frequency, $\Omega = 1.15$, has supersonic tip speed and radiation is stronger.

Ducted Rotor

For the ducted rotor, the computational domain is shown in Figure 13. The discretization process is identical to the previous case except now an infinitely thin duct wall is placed at r = 1 for $-4 \le x \le 8$.

When the rotor is placed inside the duct, very little sound will be radiated because both frequencies are cut-off. Figure 14 shows the pressure contours at t=10, 20, 45, 100. It shows that the intensity of sound radiation decreases dramatically after the initial transient state. Pressure history is shown in Figure 15 and no time periodic solution is found.

Generation and Radiation of Acoustic Waves from a 2-D Shear Layer

In this problem, a point source is placed inside a 2-D jet and acoustic radiation is to be computed. The governing equations are the linearized Euler equations,

$$\frac{\partial \rho'}{\partial t} + \bar{u}(y)\frac{\partial \rho'}{\partial x} + \bar{\rho}(y)\frac{\partial u'}{\partial x} + \bar{\rho}(y)\frac{\partial v'}{\partial y} + \frac{d\bar{\rho}}{dy}v' = 0$$

$$\frac{\partial u'}{\partial t} + \bar{u}(y)\frac{\partial u'}{\partial x} + \frac{1}{\bar{\rho}(y)}\frac{\partial p'}{\partial x} + \frac{d\bar{u}}{dy}v' = 0$$

$$\frac{\partial v'}{\partial t} + \bar{u}(y)\frac{\partial v'}{\partial x} + \frac{1}{\bar{\rho}(y)}\frac{\partial p'}{\partial y} = 0$$

$$\frac{\partial p'}{\partial t} + \bar{u}(y)\frac{\partial p'}{\partial x} + \frac{\partial u'}{\partial x} + \frac{\partial v'}{\partial y} = Ae^{-B(\ln 2)(x^2 + y^2)}\cos(\Omega t)$$
(15)

In the present calculation, the variables are non-dimensionalized by the mean values at the jet centerline, namely, the speed of sound a_j for the velocity, ρ_j for density and $\rho_j a_j^2$ for the pressure. The parallel mean velocity profile is,

$$\bar{u}(y) = \begin{cases} M_j e^{-(\ln 2)\left(\frac{|y|-h}{b}\right)^2}, & |y| \ge h\\ M_j, & |y| \le 0 \end{cases}$$

$$(16)$$

and the mean density is obtained by the Crocco's relation. Mach number of the jet $M_j=2$. The other parameters are $A=1,\,B=8,\,h=0.6$ and b=0.4.

The computational domain of $[-8, 54] \times [0, 12]$ is shown in Figure 16. Due to symmetry in the mean flow and the source term, only the solution in the upper half plane is computed. Symmetry condition is applied for ρ' , u' and p' and antisymmetry condition is applied for v'.

As indicated in Figure 16, supersonic and subsonic non-reflecting boundary conditions are treated differently. By (16), mean flow is supersonic for |y| < 1. At supersonic inflow, all variables are set to be zero and at supersonic outflow, backward difference is used for all the spatial derivatives in (15). At subsonic non-reflecting boundaries, the following PML equations are used [9],

$$\frac{\partial \rho'_{1}}{\partial t} + \sigma_{x}\rho'_{1} + \bar{u}(y)\frac{\partial \rho'}{\partial x} + \bar{\rho}(y)\frac{\partial u'}{\partial x} = 0$$

$$\frac{\partial \rho'_{2}}{\partial t} + \sigma_{y}\rho'_{1} + \bar{\rho}(y)\frac{\partial v'}{\partial y} + \frac{d\bar{p}}{dy}v' = 0$$

$$\frac{\partial u'_{1}}{\partial t} + \sigma_{x}u'_{1} + \bar{u}(y)\frac{\partial u'}{\partial x} + \frac{1}{\bar{\rho}}\frac{\partial p'}{\partial x} = 0$$

$$\frac{\partial u'_{2}}{\partial t} + \sigma_{y}u'_{2} + \frac{d\bar{u}}{dy}v' = 0$$

$$\frac{\partial v'_{1}}{\partial t} + \sigma_{x}v'_{1} + \bar{u}(y)\frac{\partial v'}{\partial x} = 0$$

$$\frac{\partial v'_{2}}{\partial t} + \sigma_{y}v'_{2} + \frac{1}{\bar{\rho}}\frac{\partial p'}{\partial y} = 0$$

$$\frac{\partial p'_{1}}{\partial t} + \sigma_{x}p'_{1} + \frac{\partial u'}{\partial x} = 0$$

$$\frac{\partial p'_{2}}{\partial t} + \sigma_{y}p'_{2} + \frac{\partial v'}{\partial y} = 0$$
(17)

where σ_x and σ_y are the absorption coefficients. A more detailed and general formulation for non-uniform mean flow is given in [9]. The width of the PML domain is 2 at the top and left radiation boundaries and 4 at the right outflow boundary for better absorption of the growing instability waves.

A uniform grid is used in x with $\Delta x = 0.1$ while a non-uniform grid is used in y for an increased resolution inside the shear layer. The grid size in y is such that $\Delta y = 0.025$ for 0 < y < 2, $\Delta y = 0.05$ for 2 < y < 3 and $\Delta y = 0.1$ for 3 < y < 12. Again, the spatial derivatives are approximated by the optimized 7-point central difference scheme (DRP in [6]), time integration by LDDRK56 [7] and a tenth-order explicit filter is applied throughout the computational domain for the elimination of short waves that are not resolved in the discretization [9].

Instantaneous pressure contours are shown in Figure 17 for the two frequencies specified in the problem, $\Omega=0.28\pi$ (St= $\frac{2fR_{1/2}}{u_j}=0.14$) and $\Omega=1.2\pi$ (St=0.6), respectively. Since the shear layer is unstable in the low frequency case, the excitation of the instability wave results in stronger sound radiation. This is also seen in the instantaneous pressure profile along y=1 (the center of the shear layer), shown in Figure 18, and \bar{p}^2 along y=10, shown in Figure 19. Indeed, in an earlier calculation where the values of h and b were inadvertently interchanged, which results in a larger shear layer thickness, the growth of instability wave was much smaller and the sound radiation weaker.

REFERENCES

- [1] F. Q. Hu, M. Y. Hussaini and J. L. Manthey, "Application of low dissipation and dispersion Runge-Kutta schemes to benchmark problems in computational aeroacoustics", *Benchmark Problems In Computational Aeroacoustics*, NASA CP 3300, 73-98, 1995.
- [2] F. Q. Hu and J. L. Manthey, "Application of PML absorbing boundary conditions to the Benchmark Problems of Computational Aeroacoustics", *Second Computational Aeroacoustics (CAA) Workshop on Benchmark Problems*, NASA CP 3352, 119-151, 1997.
- [3] K. W. Thompson, "Time dependent boundary conditions for hyperbolic systems", Journal of Computational Physics, Vol. 68, 1-24, 1987.
- [4] T. Z. Dong and R. R. Mankbadi, "Numerical simulations of small amplitude acoustic wave propagation in a converging-diverging nozzle, *Benchmark Problems In Computational Aeroacoustics*, NASA CP 3300, 285-290, 1995.

- [5] C. K. W. Tam, "Computational Aeroacoustics: Issues and methods", AIAA Journal, Vol. 33, 1788-1796, 1995.
- [6] C. K. W. Tam, T. Z. Dong and K. A. Kurbatskii, "Multi-size-mesh, multi-time-step computational algorithm", AIAA paper 99-1850, 1999.
- [7] F. Q. Hu, M. Y. Hussaini, J. L. Manthey, "Low-dissipation and -dispersion Runge-Kutta schemes for computational acoustics", Journal of Computational Physics, Vol. 124, 177-191, 1996.
- [8] F. Q. Hu, "On absorbing boundary conditions for linearized Euler equations by a perfectly matched layer", Journal of Computational Physics, Vol. 129, 201-219, 1996.
- [9] F. Q. Hu, "On Perfectly Matched Layer as an absorbing boundary condition", AIAA paper 96-1664, 1996.

FIGURES

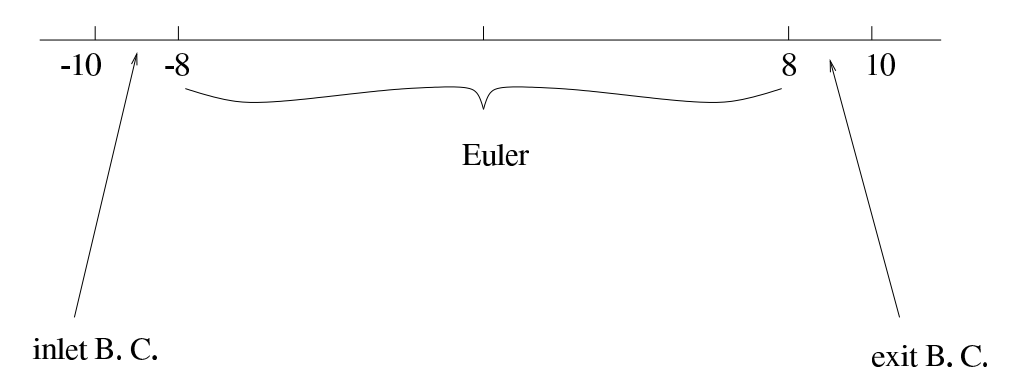


Figure 1. Schematic of computational domain partitions.

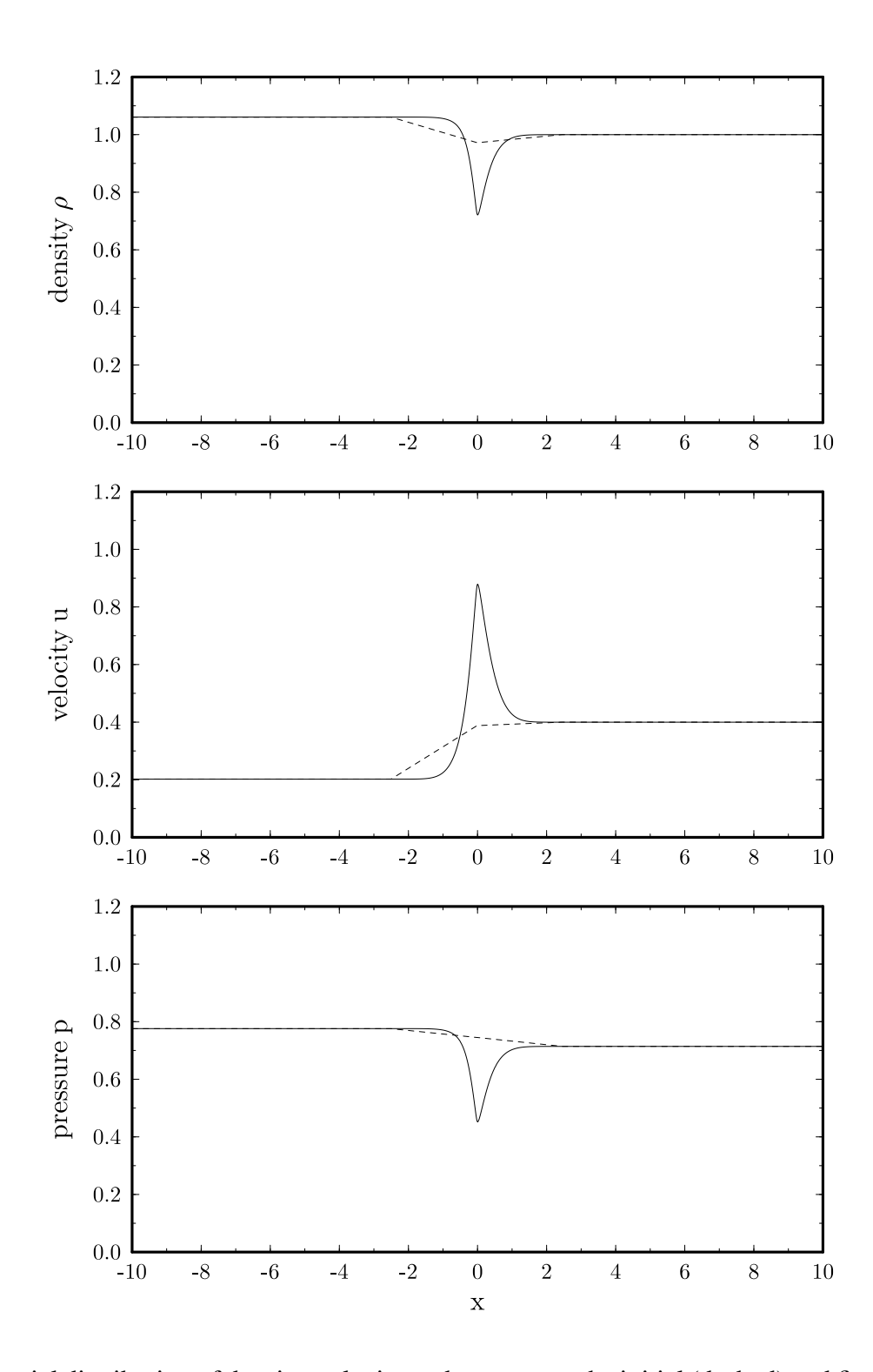


Figure 2. Spatial distribution of density, velocity and pressure at the initial (dashed) and final (solid) stages.

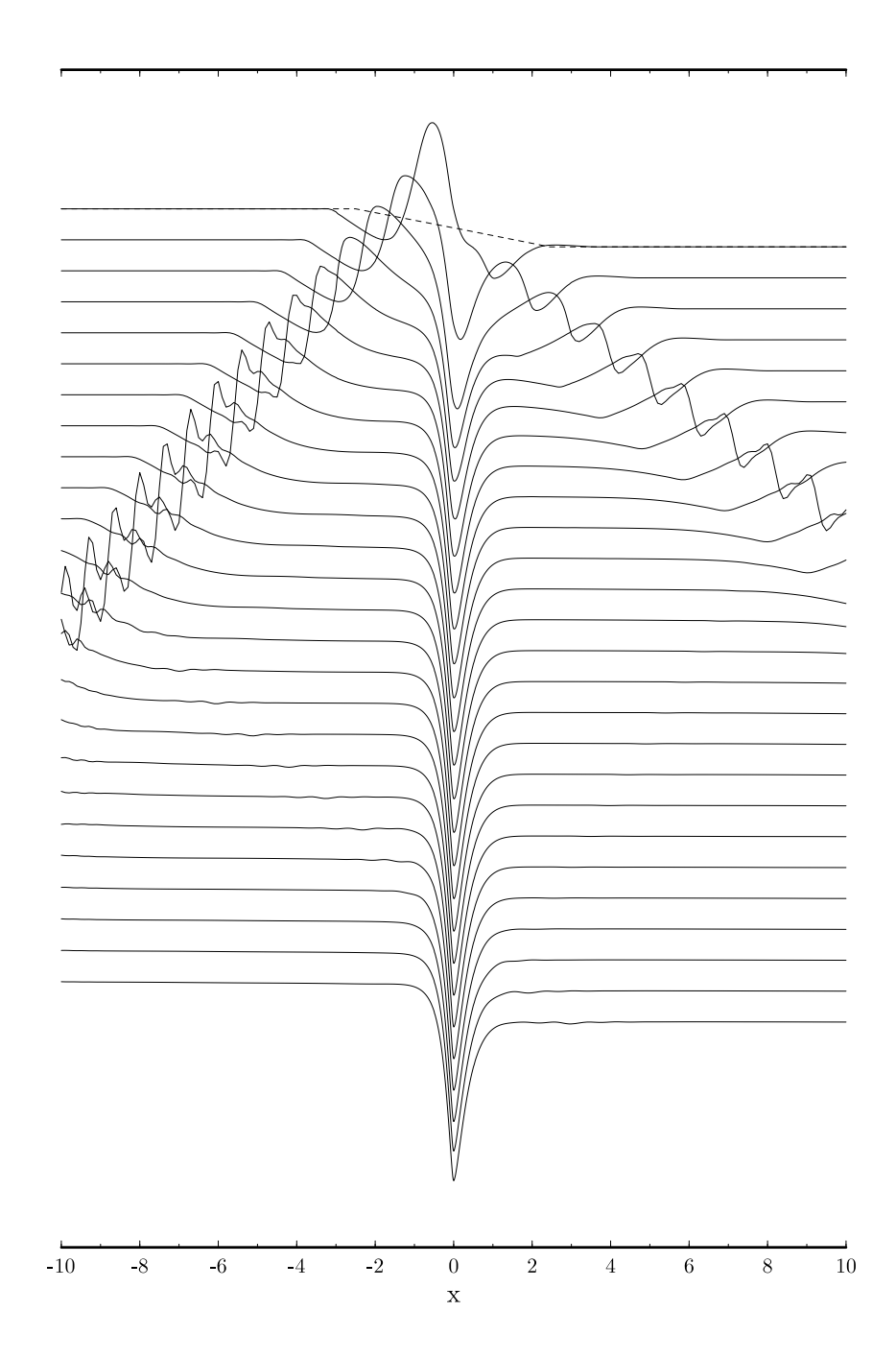


Figure 3. Time history of the pressure distribution showing the propagation of the initial transient variations.

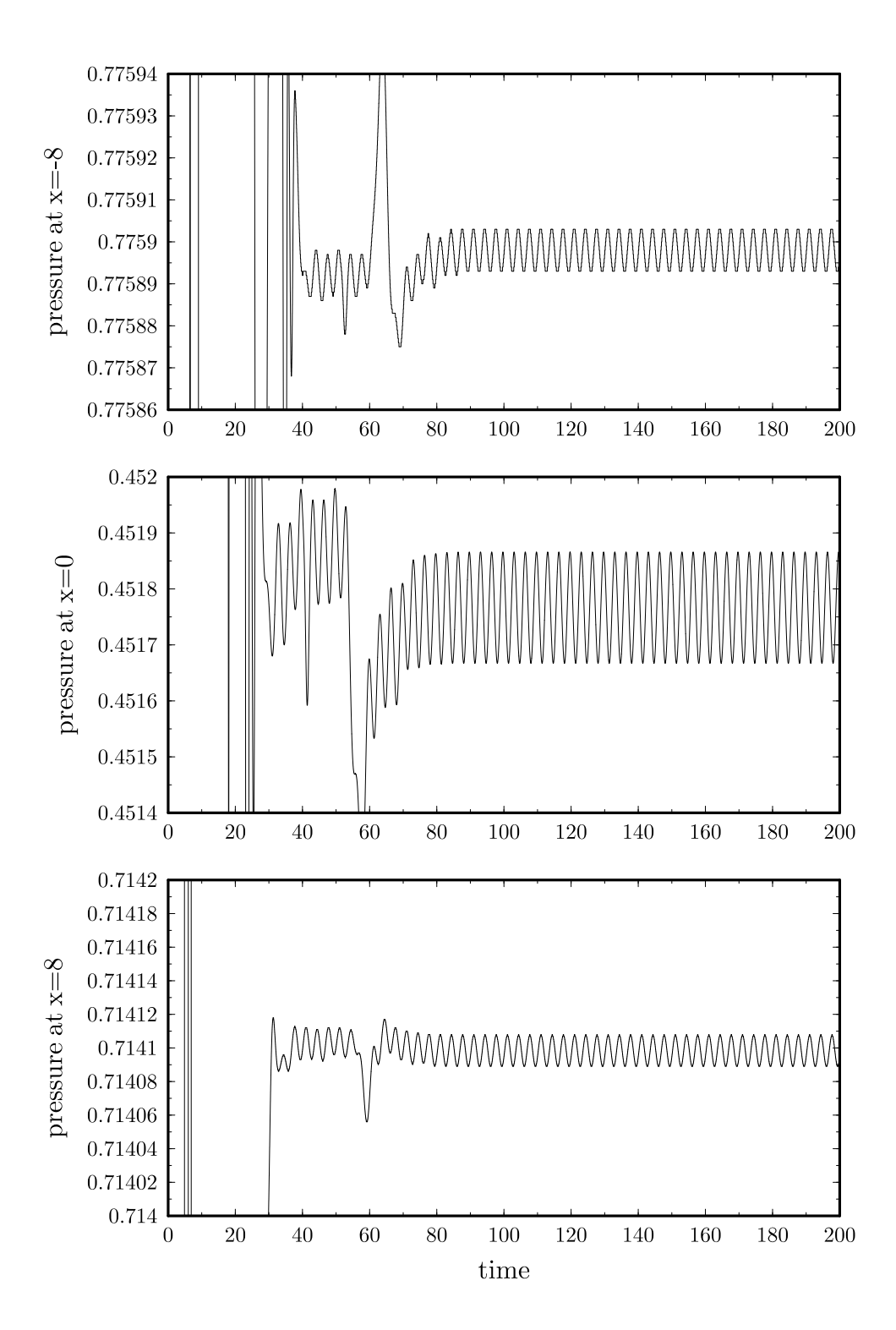


Figure 4. Pressure as a function of time at x = -8, 0 and 8 respectively.

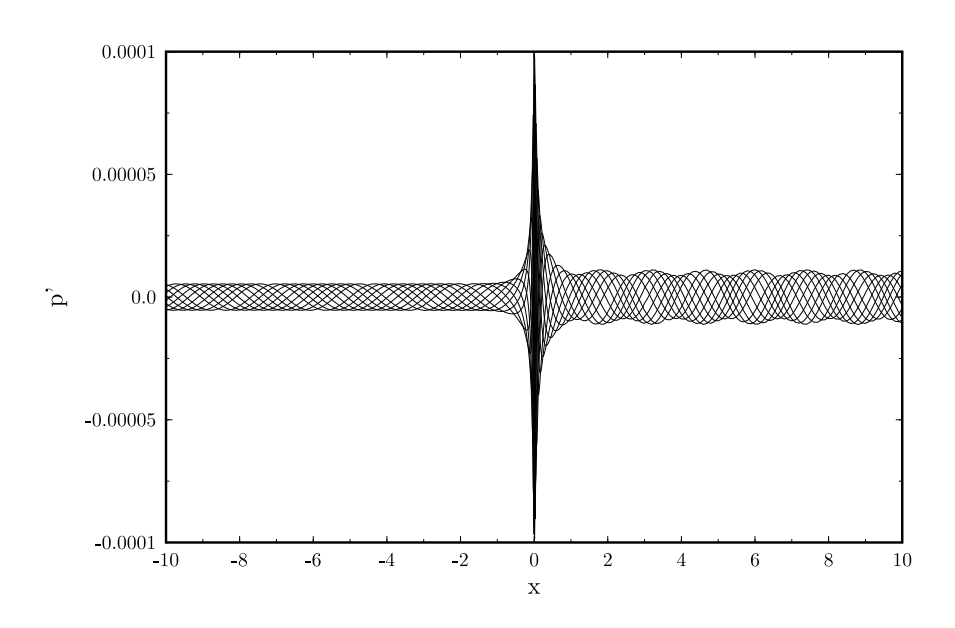


Figure 5. Pressure as a function of x spanning a period, showing the wave envelope.

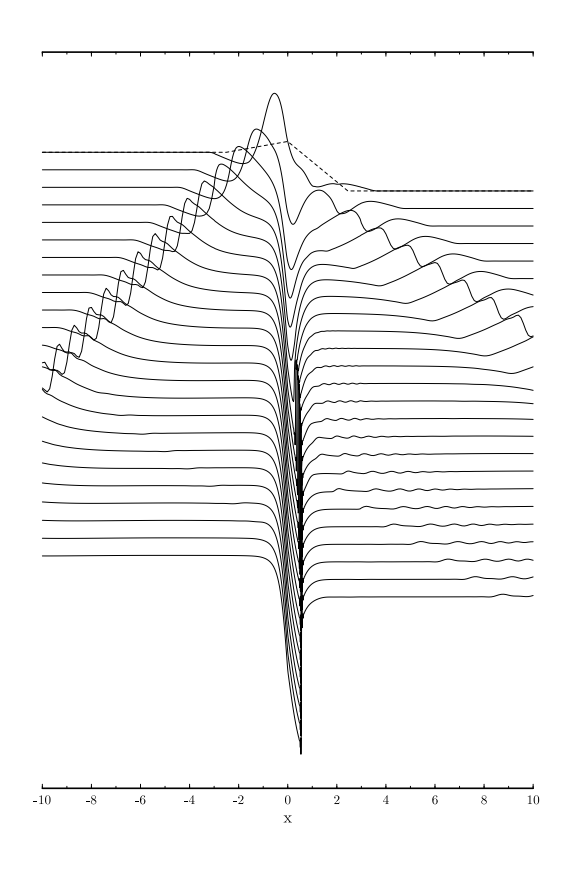


Figure 6. Time history of pressure as a function of x, showing the formation of shock from the initial profile (dashed).

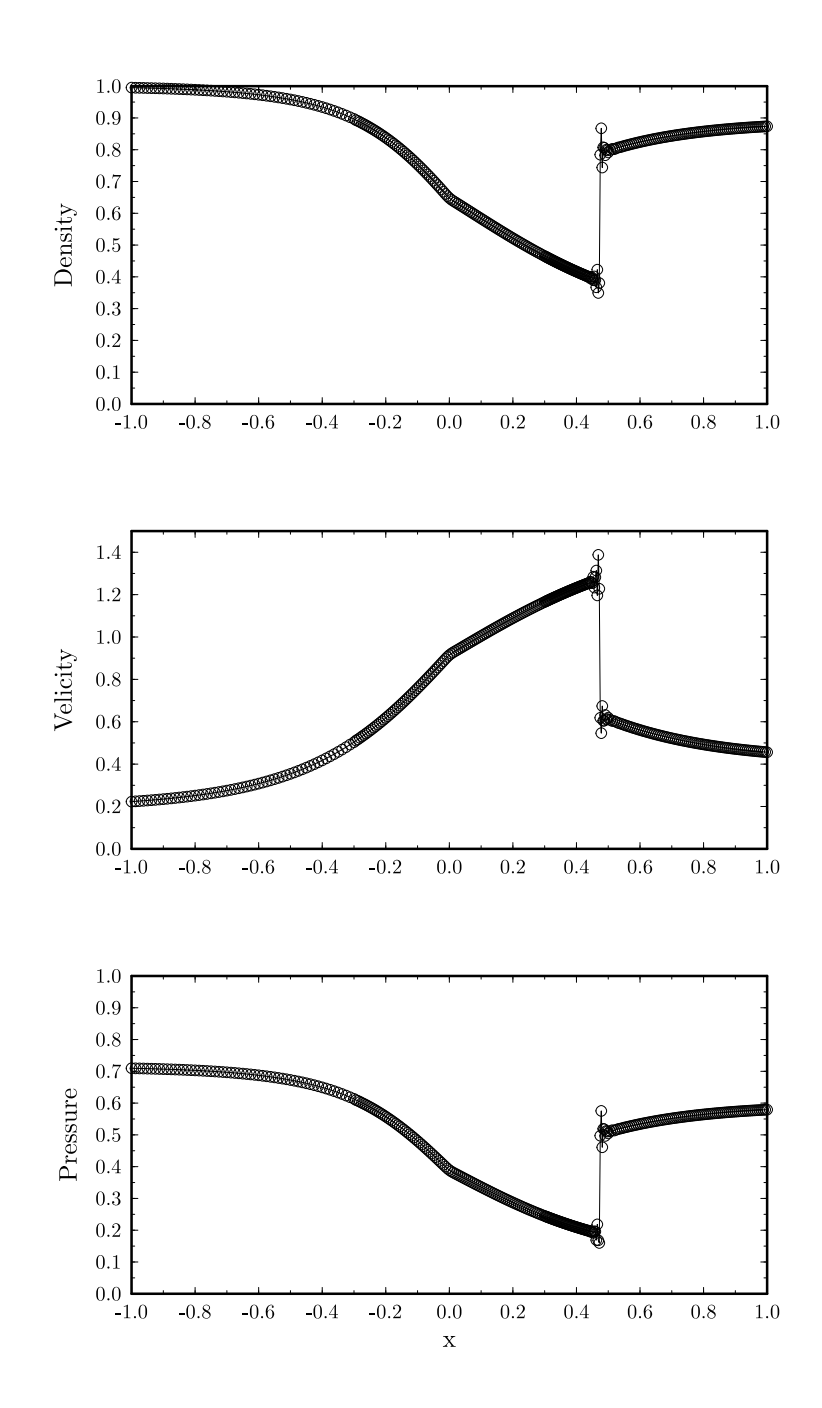


Figure 7. Final stage of density, velocity and pressure.

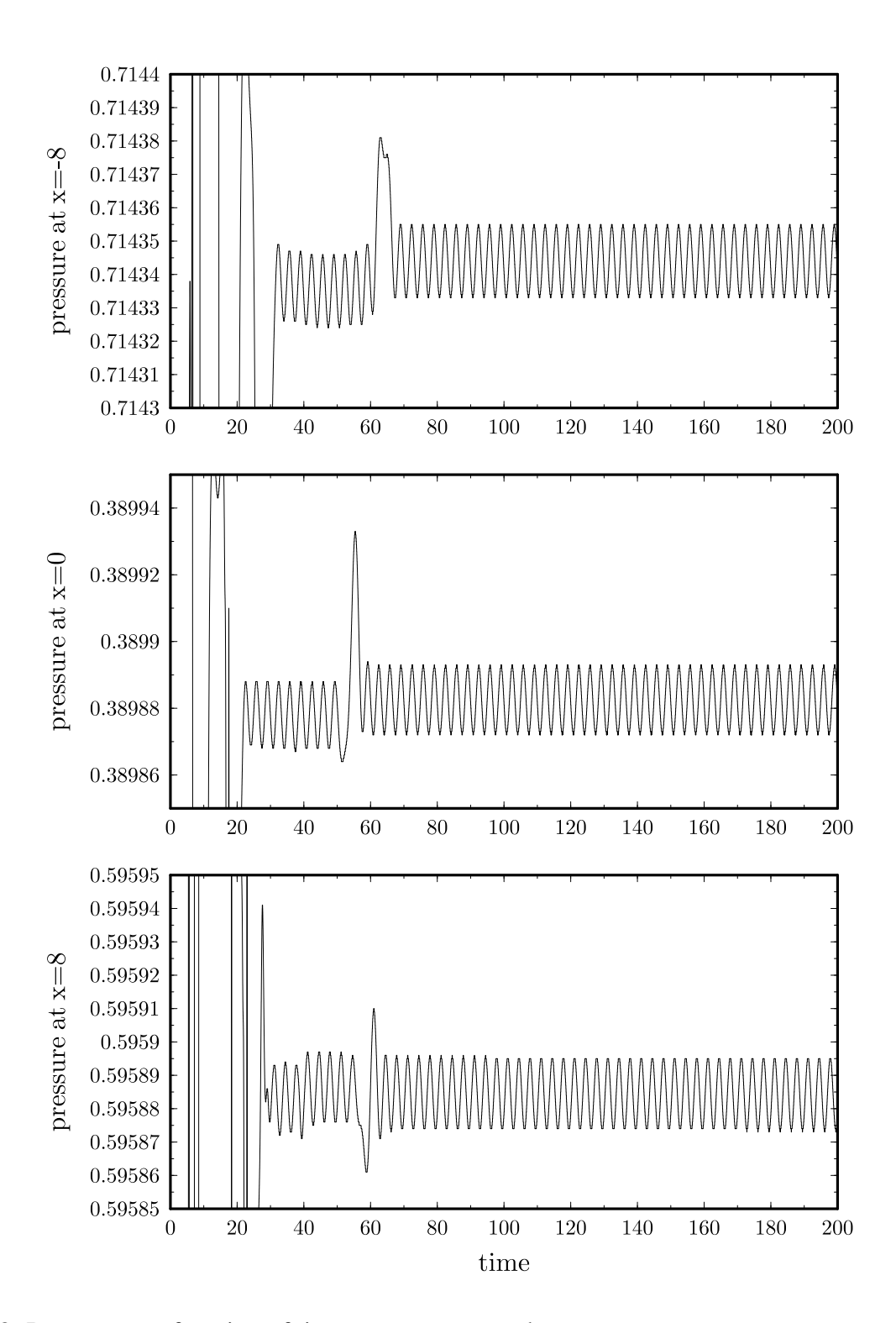


Figure 8. Pressure as a function of time at x = -8, 0 and 8.

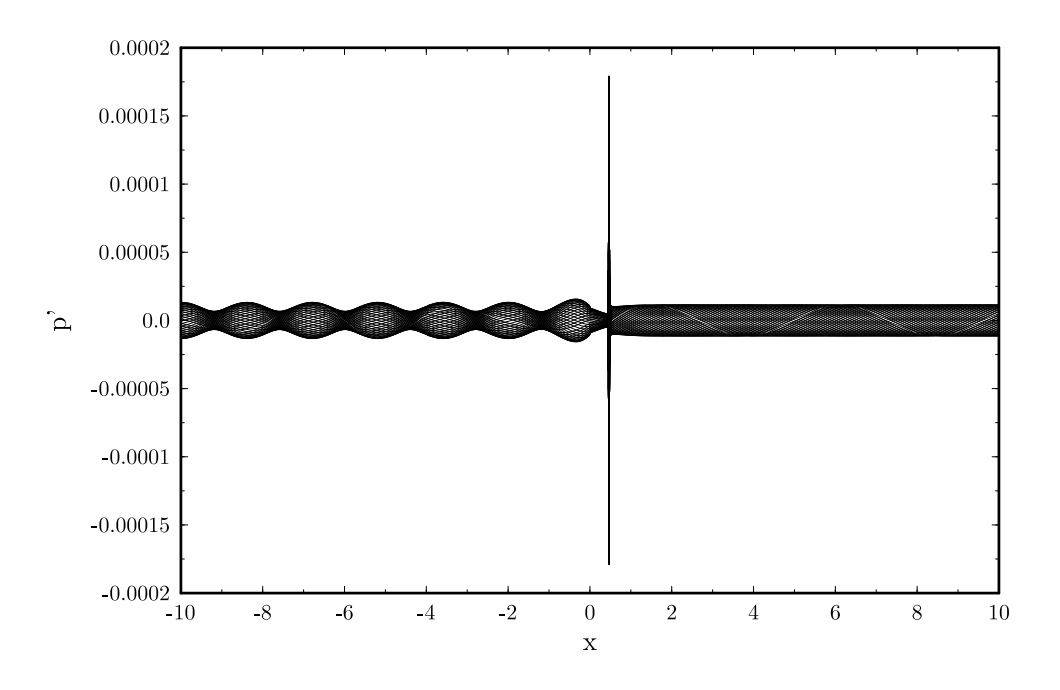


Figure 9. Pressure as a function of x at selected time steps spanning a period, showing the wave envelope.

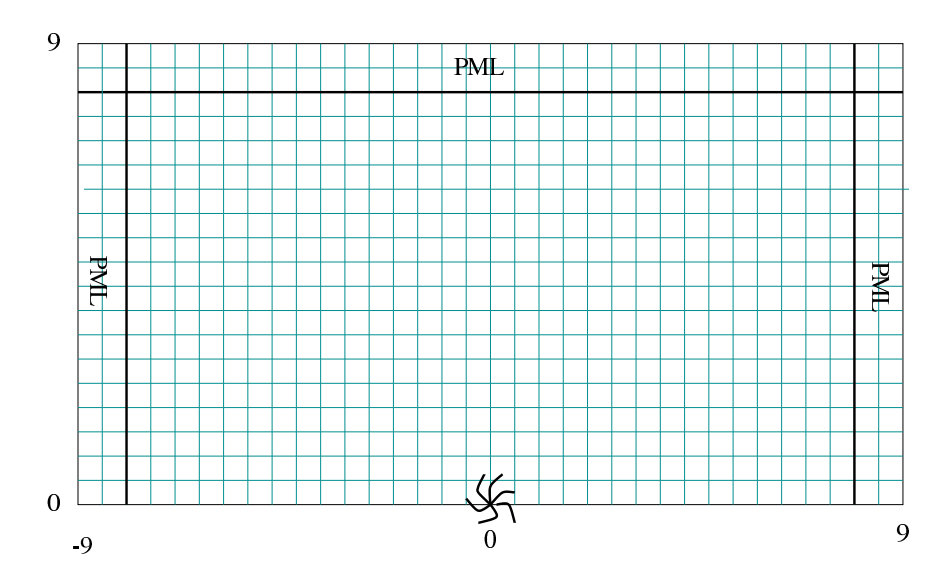


Figure 10. Computational domain for open rotor, showing the PML domains at non-reflecting boundaries.

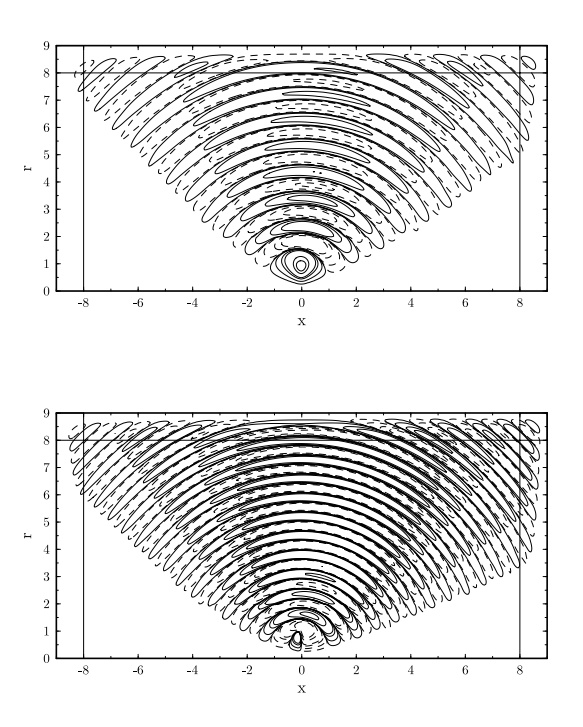


Figure 11. Pressure contours for (a) $\Omega=0.85$, (b) $\Omega=1.15$.

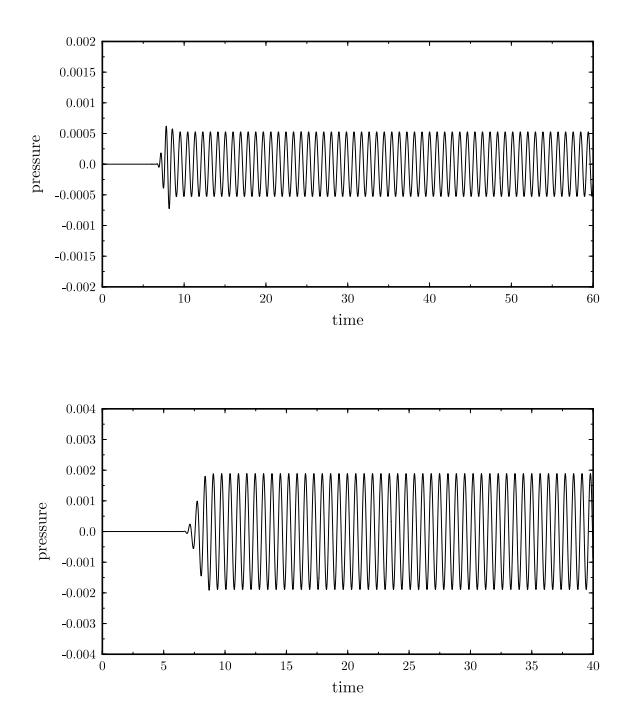


Figure 12. Pressure as a function of time at (0, 8.5), (a) $\Omega = 0.85$, (b) $\Omega = 1.15$.

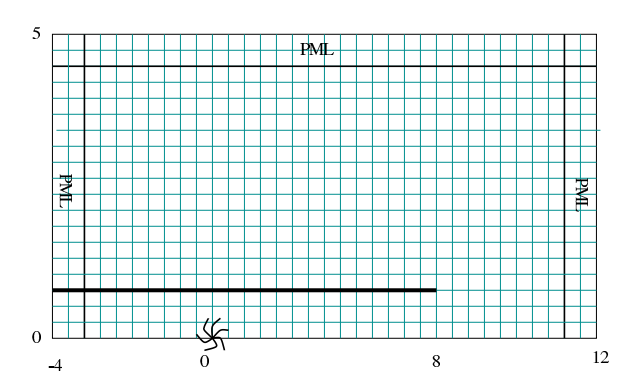
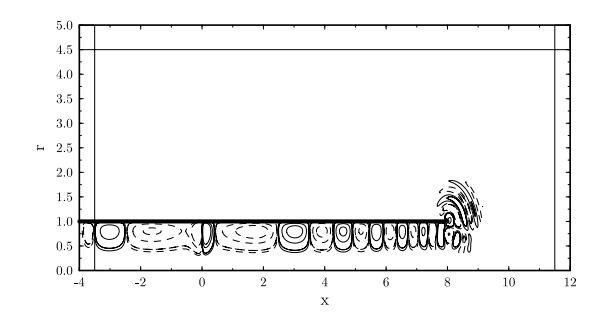
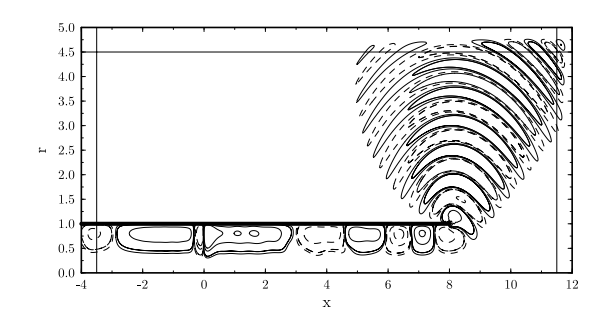
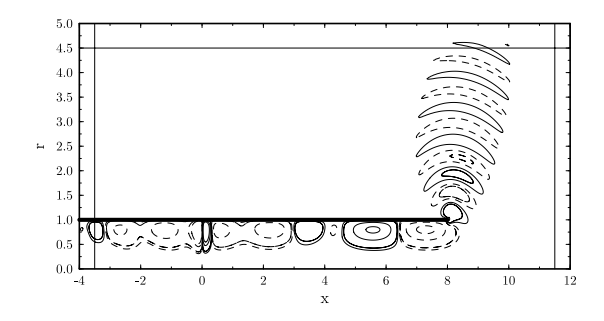


Figure 13. Computational domain for ducted rotor.







(continued next page)

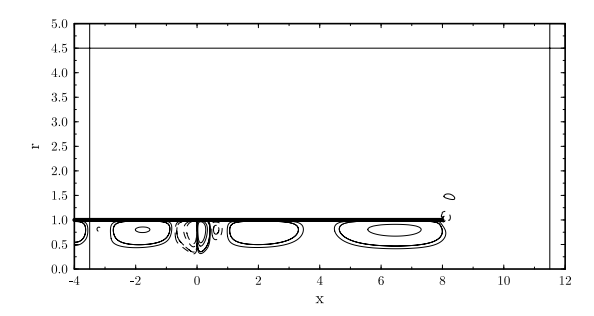


Figure 14. Pressure contours at t = 10, 20, 35, 100.

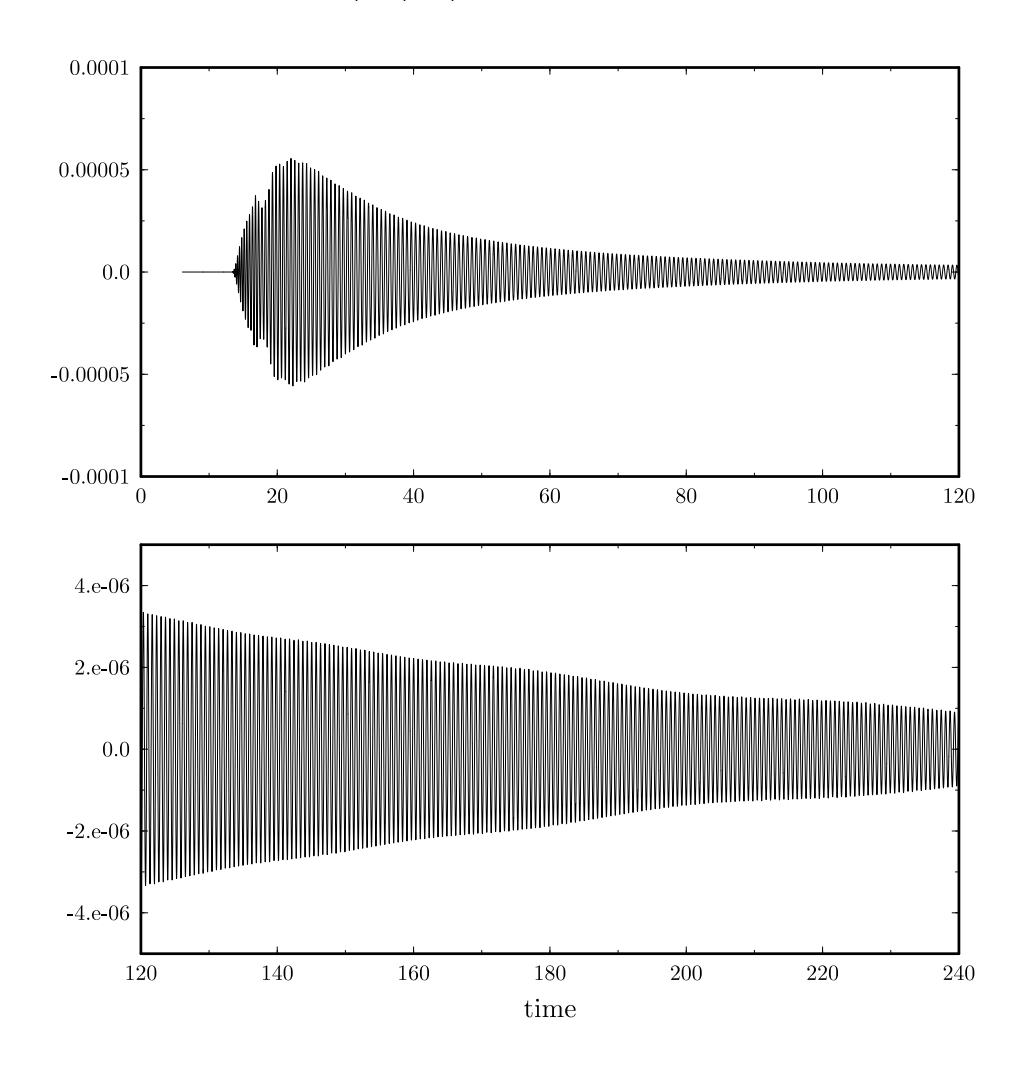


Figure 15. Pressure as a function of time at (0, 8.5). $\Omega = 0.85$. No time periodic solution is found.

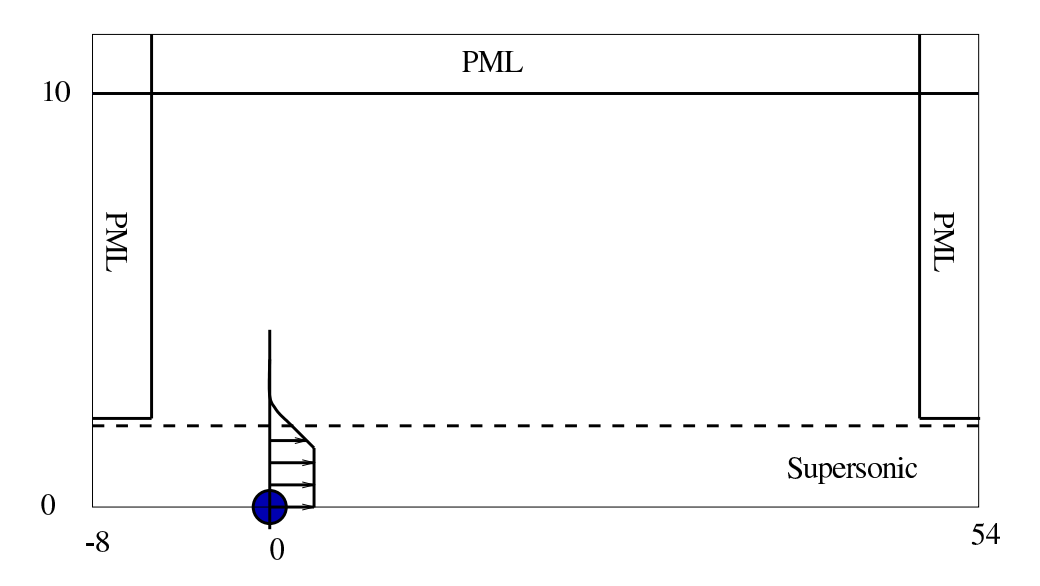
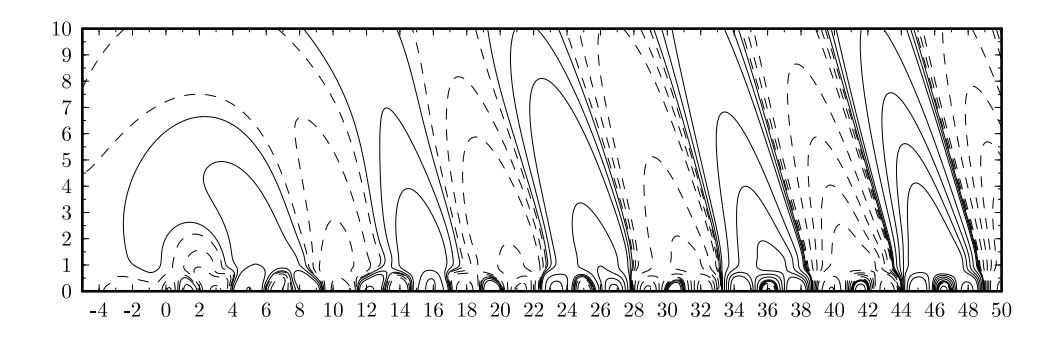


Figure 16. A schematic of computational domain showing the use of PML domains at all the subsonic non-reflecting boundaries.



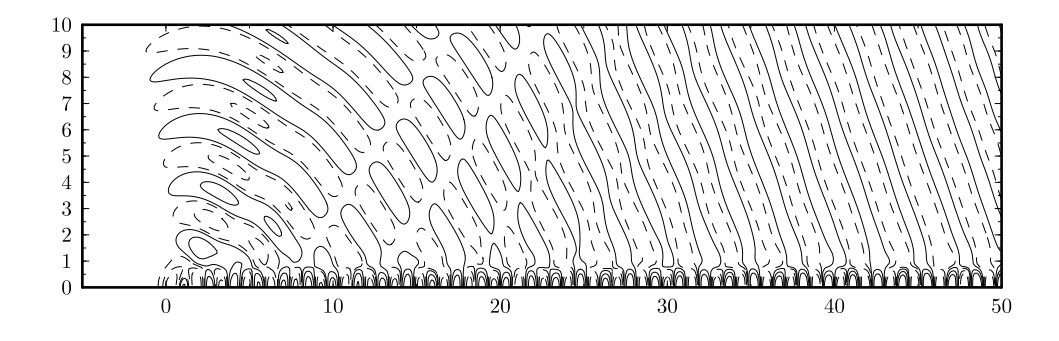


Figure 17. Instantaneous pressure contours for $\Omega = 0.28\pi (\text{top})$ and $\Omega = 1.2\pi (\text{bottom})$.

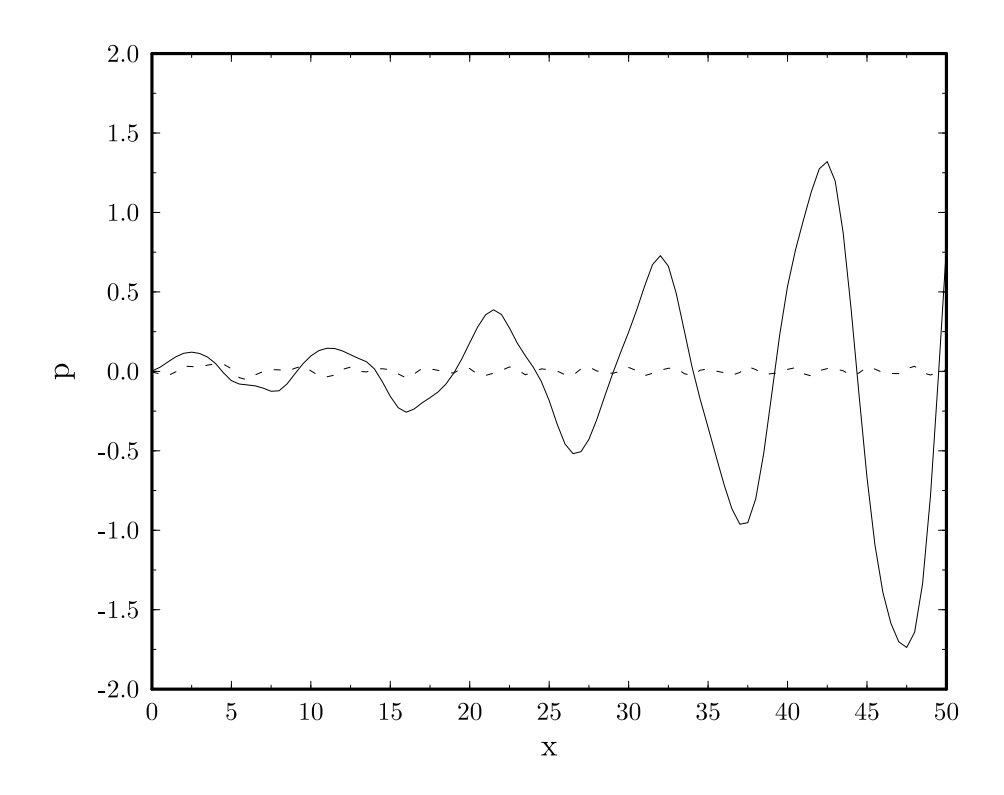


Figure 18. Pressure profile along y=1 for $\Omega=0.28\pi$ (solid) and $\Omega=1.2\pi$ (dashed).

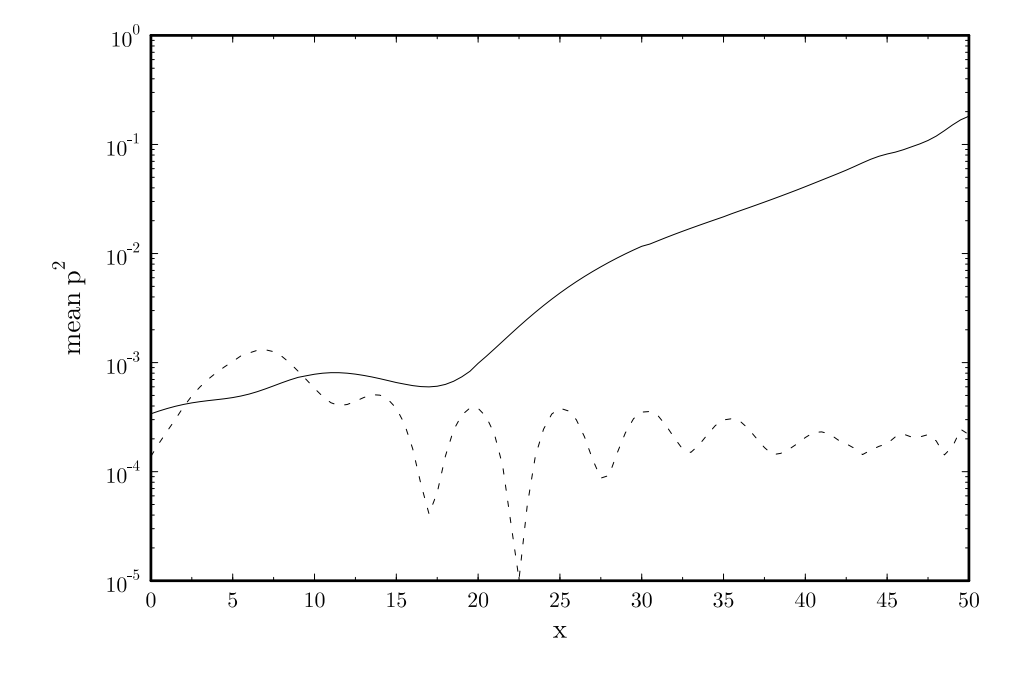


Figure 19. Mean p^2 along y=10 for $\Omega=0.28\pi$ (solid) and $\Omega=1.2\pi$ (dashed).